Quasi-open circuit response times of single- and multi-junction InGaAs photonic power converters

View Online   Export Citation   CrossMark

Osbel Almora,[1,a] Alexandre W. Walker,[2] D. Paige Wilson,[3] Carmine Pellegrino,[4] Meghan N. Beattie,[3] Lluis F. Marsal,[1] David Lackner,[4] Henning Helmers,[4] and Karin Hinzer[3,a]

AFFILIATIONS

[1]Department of Electrical and Automatic Electronic Engineering, Universitat Rovira i Virgili, Tarragona 43007, Spain
[2]Quantum Nanotechnologies Research Centre, National Research Council of Canada, Ottawa, Ontario K1A 0R6, Canada
[3]SUNLAB, Nexus for Quantum Technologies Institute, University of Ottawa, Ottawa, Ontario K1N 6N5, Canada
[4]Fraunhofer Institute for Solar Energy Systems ISE, Freiburg 79110, Germany

[a]Authors to whom correspondence should be addressed: osbel.almora@urv.cat and khinzer@uottawa.ca

ABSTRACT

Photonic power converters provide an emerging alternative to traditional metallic cabling due to their immunity to electromagnetic interference and for minimizing fire hazards as well as their ability to wirelessly power loads. In this work, we study the electrical response as a function of laser power in single and multi-junction $In_{0.53}Ga_{0.47}As$-based structures using current–voltage and impedance spectroscopy techniques. The resistance, capacitance, and quasi-open-circuit response times are discussed. Estimated values for single- and ten-junction devices were 314 and 911 ns, respectively, measured under 1520 nm laser radiation with an irradiance of 88 mW cm^{-2}. A methodology with analytical modeling is proposed for comparing single- and multi-junction devices based on the average sub-cell performance. Our analysis provides useful information for the optimization of multi-junction photonic power converters in applications where the device response time is relevant such as simultaneous power and data transfer applications.

I. INTRODUCTION

The extensive implementation of communication devices, sensors, and smart technology has created a demand for reliable power sources in electrically isolated and extreme environments. Traditional copper cabling, sensitive to electromagnetic interference and posing risks of heating and sparking, can be replaced by photonic power transmission through optical fibers which can also be beneficial for galvanic isolation.[1] This method is immune to electromagnetic interference and minimizes hazards in challenging conditions. The process involves converting electrical power to monochromatic light using, e.g., a laser, transmitting it through optical fibers or over free-space, and converting it back to electrical power using a photonic power converter (PPC).[2,3] Similar to solar cells, the PPC utilizes the photovoltaic effect to convert this laser light into electricity. However, the monochromatic nature of the light source allows to match bandgap energy of the absorber material and photon energy and, thus, minimize thermalization and transmission losses, resulting in much higher photovoltaic conversion efficiencies than conventional solar cells.[4–6] To achieve output voltages at the receiver side sufficient to power the downstream electronics without the need of step-up voltage converters, several p–n junctions can be vertically stacked and connected electrically in series by tunnel diodes using principles derived from multi-junction (MJ) solar cell technology.[7–9]

Unlike MJ solar cells, MJ PPCs have absorber layers with similar or equivalent bandgap energy (E_g) in each sub-cell.[3] The absorber layer thicknesses are carefully designed for each sub-cell to generate the same photocurrent for operation in current-matched conditions. State-of-the-art PPC devices composed of III–V semiconductors have demonstrated monochromatic power conversion efficiencies (PCEs) approaching 70%.[10] Single-junction GaAs devices have demonstrated a record efficiency of 68.9% leveraging optical resonance effects.[11] GaAs-based PPCs have also shown efficiencies well above 50% even at high irradiances of 500 W cm^{-2} (0.5 mm diameter devices)[12] and input powers above 60 W (1 cm^2 devices).[13]

Moreover, PPCs designed for operations in the telecom range starting from the O-band near 1310 nm and ideally closer to 1550 nm could enable long-distance transmission up to tens of km due to minimal fiber attenuation. These longer wavelengths, however, require smaller bandgap materials such as $In_{0.53}Ga_{0.47}As$ (InGaAs in the remainder of this manuscript) or InGaAsP lattice matched to InP.[14–16]

Due to the advantages associated with optical power transmission, there is an increasing interest in utilizing existing telecommunication optical networks for the dual purpose of simultaneous power and data transmission.[17] This concept holds significant potential for transforming systems where both power delivery and communication capabilities are essential, such as in sensor networks and medical instrumentation.

The electrical characterization of PPCs is usually done in the direct current (DC) mode, in which the device electrical response is measured in steady-state conditions.[18] Typically, current density–voltage (J–V) measurements under nominal illumination conditions are used to assess the PCE and related device performance parameters. Although effective for DC operation, this approach is not suited for studying the characteristic response times of the samples, which are relevant for data transmission purposes.

Understanding the time-dependent characteristics of the device's electrical response requires transient and/or alternating current (AC) mode methods. In the latter case, impedance spectroscopy[19,20] is an effective technique which provides insights not only on the resistive energy dissipation which influences efficiency but also on the

capacitive energy storage kinetics. The resistive–capacitive coupling defines the transport properties for data transmission in PPC applications. Specifically, impedance spectroscopy measurements can be performed in several conditions to assess the corresponding response time τ behavior of the PPCs.[21]

In this article, DC and AC approaches are integrated to investigate fundamental device characteristics of PPCs featuring single-junction (1 J) and ten-junction (10 J) structures. Key methodologies applied encompass steady-state J–V and impedance spectroscopy spectra in the dark and under increasing laser irradiances. The conducted experiments were systematically scrutinized using the parametric Shockley equation[22] and equivalent circuit models.[23] Estimations of the characteristic response times are reported for relevant operational conditions.

II. MODELING AND EXPERIMENTAL

A. PPC models

The illustrations in Fig. 1(a) depict the simplified structures of a single-junction (1 J) and a ten-junction (10 J) PPC. For the MJ device, each sub-cell is represented as a p^+–n junction realized with the given absorber material. Tunnel diodes interconnect each sub-cell and are assumed to have negligible ohmic conductivity and high optical transparency; these structures have recently been made transparent for PPCs, targeting 1550 nm laser wavelengths using higher bandgap materials.[24]
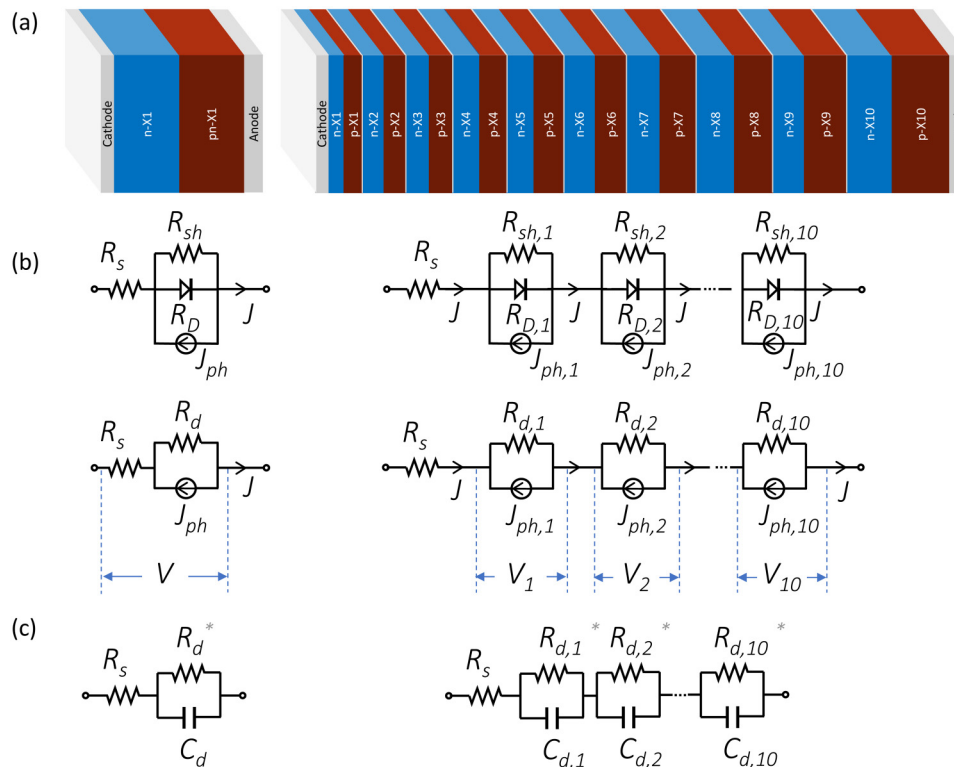

FIG. 1. Schemed device (a) layer structure, and equivalent circuits in (b) direct and (c) alternating current modes for the single-junction (left), and ten-junction (right) samples. In (b), the same circuit is represented above and below, separating shunt R_{sh} and diode R_D resistances and representing the equivalent device resistance R_d, respectively. In (c), the gray asterisk indicates that the device resistance is only the same in DC and AC, if no series connection of resistive–capacitive branches is present. All equivalent circuits neglected tunnel junctions.

Figure 1(b) illustrates simplified DC equivalent circuits for 1 and 10 J devices. Regardless of the configuration, the parasitic series resistance (R_s) accounts for ohmic voltage losses, but depending on the junction, the ith sub-cell can be simulated with a parallel connection of parasitic shunt resistance ($R_{sh,i}$), voltage-dependent diode recombination nonlinear resistance ($R_{D,i}$), and photocurrent ($J_{ph,i}$). The same circuit can also be represented [shown below in Fig. 1(b)] using the equivalent voltage-dependent nonlinear device resistance $R_{d,i}$ which accounts for the parallel connection of shunt and diode resistances, $R_{d,i} \approx R_{sh,i}R_{D,i}/(R_{sh,i} + R_{D,i})$. For operating conditions where the diode resistance is much smaller than the shunt resistance ($R_{D,i} \ll R_{sh,i}$), this simplifies to $R_{d,i} \cong R_{D,i}$. This more "condensed" form of the DC equivalent circuit is introduced as a visual bridge between the traditional representation (with the diode symbol emphasizing current flow) and the resistor-element-focused AC circuit.

Figure 1(c) presents simplified AC equivalent circuits for 1 and 10 J junction devices in terms of linear equivalent circuit elements. For instance, the ith sub-cell can be simulated with a parallel connection of a device resistance ($R_{d,i}$) and capacitance ($C_{d,i}$). Even though the equivalent circuits of Fig. 1(c) are arguably over-simplifications of more complex models with multiple resistive, capacitive, and even inductive contributions, they describe the fundamental device time response, i.e., the ith sub-cell will respond to a small perturbation with a characteristic effective relaxation time $\tau_i = R_{d,i}C_{d,i}$ as long as resistances and capacitances can be effectively defined per sub-cell. The applicability of this model may be limited in real devices, where capacitive elements often behave as constant-phase elements and resistive terms may include leakage pathways. In such cases, the system exhibits a distribution of time constants, making the parallel RC representation only a lumped-element approximation, and the extracted τ may not directly correspond to a single physical process.[25] Notably, an asterisk is used for the $R_{d,i}$ elements in the equivalent circuit of Fig. 1(c). This notation emphasizes two points: first, the transition of the device resistance from a nonlinear to a linear form under the tested DC operating point with small perturbations, in contrast to the representations in Fig. 1(b); and second, that DC and AC resistances may differ due to capacitive or inductive circuit branches, which do not contribute to the low-frequency limit in the DC regime.

B. PPC fabrication

Monolithic 1 and 10 J PPCs based on InGaAs absorber material with a bandgap of $E_g = 0.736$ eV were fabricated at Fraunhofer ISE.[26,27] The devices were grown lattice matched on 4-in. InP wafers by metal-organic vapor phase epitaxy (MOVPE) with standard precursor and reactor conditions.[28] Each individual sub-cell consists of an absorber layer sandwiched between high-bandgap barrier layers providing front (FSF) and back surface fields (BSF) for improved carrier collection efficiency. The absorption coefficient of the absorber material was reported elsewhere.[27,29]

The 1 J PPC features an absorber thickness of 540 nm. This structure was intended as a test structure for absorption calibration and is by design only partially absorbing. From an optical simulation of the PPC performed with the transfer matrix

method,[30] the absorptance at 1520 nm is 36%. In the 10 J case, the absorber thicknesses of the individual sub-cells were optimized to achieve current-matching conditions and an estimated absorption close to 90% at 1520 nm. Further details on the design can be found elsewhere.[27]

The epi-wafers were processed into 5.4-mm^2 cells (designated area, i.e., chip area minus busbars) with front and back side metallization realized with metal evaporation, photolithography, and wet chemical etching. An anti-reflective coating was designed and deposited to optimize absorption for wavelengths around 1520 nm.

C. PPC characterization

The dark $J - V$ curves were measured using an Agilent 4155C semiconductor parameter analyzer using low noise tri-axial cables with a ground floor of <100 fA. For the $C - V$ and impedance spectroscopy spectra measurements, an Agilent 4284A precision LCR meter was employed, applying an AC perturbation of 10 mV at a frequency of 10 kHz.

The light $J - V$ and $C - V$ curves under increasing irradiances were measured on a temperature-controlled stage held at 25 °C. The DC measurements were recorded with a Keithley 2400 source meter in a four-wire configuration and for the impedance spectroscopy spectra, an E4980A precision LCR meter from Keysight was employed with AC perturbations from 30 to 50 mV in the frequency range from 20 Hz to 2 MHz.

III. RESULTS AND DISCUSSION

A. Dark current–voltage characteristic

The electrical response is modeled using the DC equivalent circuits of Fig. 1(b). Assuming negligible series resistances ($R_s \cong 0$), shunt resistance can be considered with the empirical form of Shockley's equation[22] to express the dark current throughout a single-junction device as

$$J = J_0 \left(\exp\left[\frac{q\,V}{mk_BT}\right] - 1 \right) + \frac{V}{R_{sh}}, \qquad (1)$$

where k_B is the Boltzmann constant; T the temperature; and m and J_0 are the ideality factor and the diode saturation current density, respectively. We consider sub-cells with similar junction characteristics, i.e., all equivalent sub-cell resistances of the 10 J device under investigation are the same ($\forall R_{d,i},\ R_{d,i} = R_{d,i+1}$). In this case, the external voltage V evenly distributes among N sub-cells, so that each junction operates at the same voltage,

$$V_1 = V_2 = \ldots = V_N = \bar{V} = \frac{V}{N}. \qquad (2)$$

Assuming also a similar shunt resistance for each sub-cell, Eq. (1) can be used to describe the current in the N-junction device with V replaced by $\bar{V}$. The assumption of equal sub-cells allows the normalization of related parameters such as the ideality factor and the resistance, which is useful for comparison purposes between single- and multi-junction devices. Therefore, the individual sub-cell ideality factor[31] in an N-junction device can be obtained from the

measured current–voltage characteristic as the average value,

$$\bar{m} = \frac{q}{Nk_BT}\left(\frac{\mathrm{dLn}\left[\hat{J}\right]}{\mathrm{d}V}\right)^{-1}, \qquad (3)$$

where the hat symbol indicates the dimensionless value of the current density $\hat{J} = J/J_u$, with $J_u = 1$ A cm^{-2}, for convenient numerical calculus after simplification of the J/J_0 argument inside the logarithm. Moreover, from the DC equivalent circuit of Fig. 1(b), the total resistance of a N-junction device can be approximated to $R = N\,\bar{R}(V)$, with $\bar{R}(V)$ being the identical sub-cell resistance in the regime $\forall R_{d,i}$, $R_{d,i} = R_{d,i+1}$. Therefore, applying the definition of differential resistance,[32] the individual sub-cell resistance in an N-Junction device can be deduced from the current–voltage characteristic as

$$\bar{R} = \left(N\frac{\mathrm{d}J}{\mathrm{d}V}\right)^{-1}. \qquad (4)$$

Note that Eq. (4) does not include effects possibly present in real devices, including sub-cells with intentionally or unintentionally poor junction properties, and/or parasitic contact junctions,[33] which can limit its validity. Nevertheless, these average properties could be useful for comparison purposes.

The $J - V$ curves as measured in dark conditions are shown in Fig. 2(a) (left axis) as functions of the normalized average voltage per sub-cell for the 1 J and the 10 J PPCs. Both samples show similar response per $\bar{V}$ with only slightly higher current values for the 10 J device compared to the 1 J in forward bias. In contrast, the 1 J cell shows nearly twice more current in reverse bias than the 10 J device.

The differential resistance in the DC operating point of the devices can be obtained by applying Eq. (4) to the experimental $J - V$ characteristics. This is presented in Fig. 2(a) (right axis) for the 1 and 10 J samples under evaluation, showing similar current and resistance values in forward bias, where both the voltage and the resistances of the 10 J sample were averaged to the junction number. This agrees with the approach of equal sub-cells in the 10 J sample.

Contrastingly, in reverse bias, two main trends are found in Fig. 2 when comparing the 1 and 10 J devices. First, both 1 and 10 J samples nearly saturate toward a similar approximate shunt resistance in this normalized illustration. A clearer analysis of this trend would require larger reverse bias ranges, to be considered in future experiments. Second, the resistance values between −0.2 and 0 V are between 1.4 and 1.9 times lower for the 1 J PPCs in comparison to the average sub-cell of the 10 J device. This difference is attributed to the one-to-one variation of device characteristics, particularly the shunt resistance, and is, therefore, not analyzed in further detail in this work.

Figure 2(b) shows the extracted ideality factors of the 1 and 10 J samples in forward bias, showing a similar magnitude and trends with values between 1.0 and 1.7 up to 0.4 V. This agrees with the approach of average sub-cell metrics. Beyond 0.4 V, the 1 J
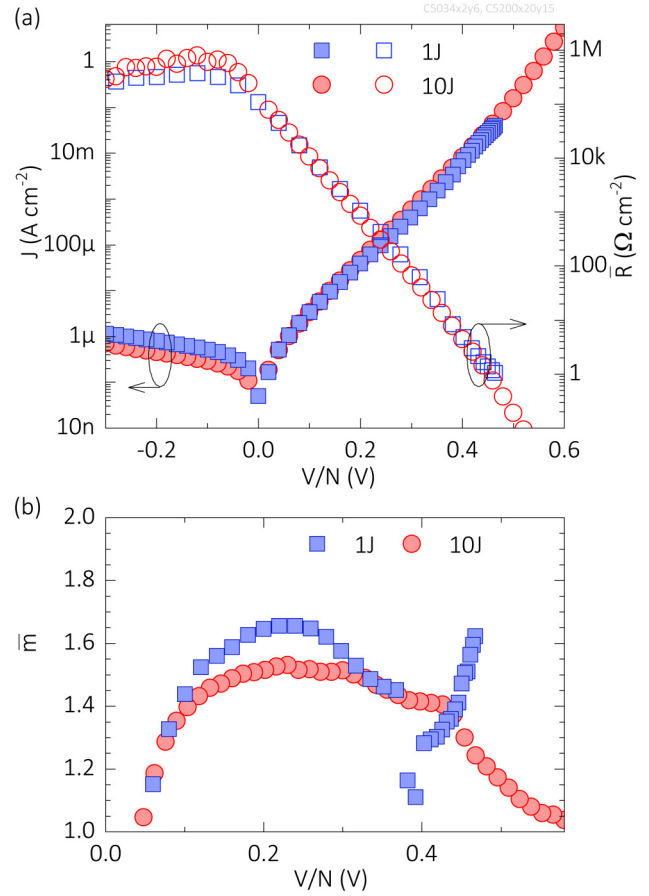

FIG. 2. (a) Dark current density J (filled symbols, left axis) and corresponding normalized resistance $\bar{R}$ (open symbols, right axis) and (b) ideality factors $\bar{m}$ as a function of the normalized junction voltage per sub-cell V/N for 1 J ($N = 1$, blue symbols) and 10 J ($N = 10$, red symbols) InGaAs PPCs.

sample's ideality factor decreases sharply toward m = 1, followed by an increase possibly due to the proximity of the onset of series resistance effects in the J–V. The 10 J sample, on the other hand, shows a steady decrease in average sub-cell ideality factor toward m = 1, as recombination in the quasi-neutral regions becomes more dominant without the onset of series resistance. The total series resistances for these samples were estimated from the impedance spectra [see Figs. 4(a)–4(c)] as ∼0.1 and ∼0.01 Ω cm^2 for the 1 and 10 J samples, respectively. Notably, the increase in series inductance—particularly at higher irradiance—not only reduces the accuracy of series resistance measurements but also requires more detailed consideration under operating conditions where the device time response is significantly influenced by series resistance.

B. Current–voltage under monochromatic irradiance

A selection of the DC measurements for the 1 and 10 J PPC samples under different irradiances are shown in Figs. 3(a) and 3(b).
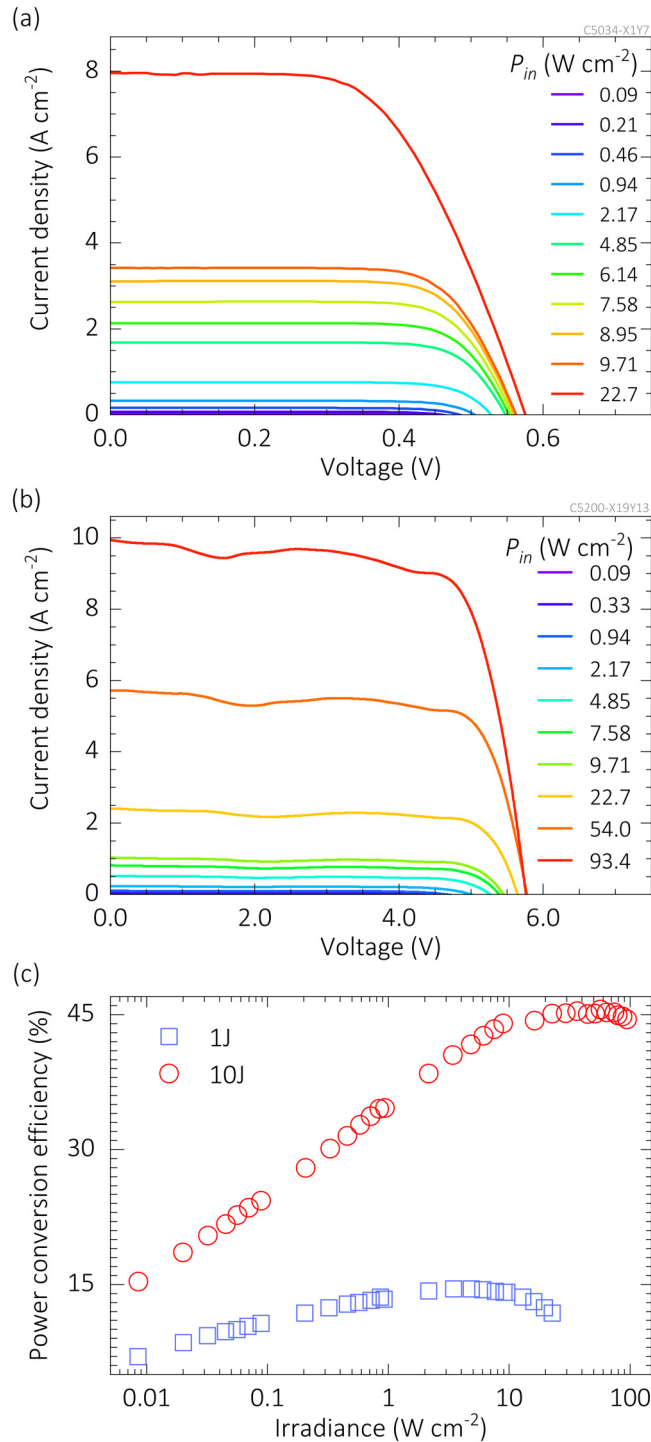
FIG. 3. Selected *J–V* curves with incident irradiances indicated from the (a) 1 J and (b) 10 J PPCs (designated area *A* = 0.054 cm²) and (c) corresponding *PCE* values under different incident irradiance values from a 1520 nm laser, as indicated in (c).

It is worth noting that the voltage of the 10 J device is effectively boosted by a factor of almost 10 with respect to the 1 J device due to the series connected nature of the device. Moreover, the 10 J device exhibits current "wiggles" in the $J - V$ curves between short-circuit condition and the maximum power point (MPP) at high irradiances. This phenomenon has been attributed to the Franz–Keldysh effect[34] on the thinner sub-cell of the structure; these are not observed in the 1 J device.

The efficiency of each of the devices as a function of laser irradiance is shown in Fig. 3(c). The 10 J device shows high efficiencies over the range of irradiances considered, with peak value of 45.7% at an irradiance of ∼54 W cm⁻². At higher irradiances, the efficiency drops. Aside from the onset of ohmic losses, in this case, this drop is also attributed to thermal management limitations of the experimental setup, which cause the cell to heat up significantly during the light $J–V$ measurement and results in a reduction in V_{oc}. The low efficiency of the 1 J PPC can be associated with the high transmission losses due to the semi-transparent thin 540 nm absorber layer of this test device.

C. Impedance spectroscopy

The devices were characterized both in dark and under monochromatic irradiance, combining DC and AC measurements. For a series of incident power density values P_{in} applied to the samples, the corresponding open-circuit voltages (V_{oc}) were recorded.[19,31] During impedance spectroscopy measurements, a DC bias equal to V_{oc} was applied so that the device operated in a quasi-open-circuit condition, ensuring that negligible DC current flowed through the sample. Under this condition, the resistive component of the impedance can be directly associated with the recombination resistance, as contributions from transport or charge extraction resistances are negligible.

On the other hand, for the capacitive component of the device impedance, the experiment is designed to probe what can be termed *flatband, diffusion* (in dark) or *chemical capacitance*. This capacitance is not only linked to forward-bias operation with applied voltages close to the built-in potential and to the maximum attainable V_{oc}, but more importantly, it reflects a capacitive signal that is no longer associated with "surface" depletion-layer capacitance. Instead, it arises from the charge-carrier "volume" modulation of the quasi-Fermi levels under small voltage perturbations. Historically,[22] such experiments were performed on p–n junctions near to or at flatband dark conditions, where diffusion current dominates over drift current. This led to the definition of the *diffusion capacitance*,[22] a capacitive contribution proportional to the diffusion current arising from field-independent quasi-Fermi level gradients. The concept was later extended to dye-sensitized solar cells under illumination at quasi-open-circuit conditions, where it was reformulated in electrochemical terms as the *chemical capacitance*[35] and subsequently applied to solid-state p–i–n solar cells as well.[36] Moreover, since the capacitance originates from charge-carrier density modulation and the resistance from recombination processes, these impedance components can be coupled through a characteristic time constant and associated with an effective charge-carrier lifetime, which has been shown to agree well with photoinduced transient photovoltage measurements.[36,37]

The $\tau = RC$ response times from impedance spectroscopy depart from the recombination lifetimes, including dielectric relaxation contribution,[38] for cases where the main capacitive response does not relate to the charge/discharge response of electronic occupation of the quasi-Fermi levels. This is true for low forward bias and reverse bias, where junction capacitance is the main contribution, and for high injection forward bias, where the low resistivity of the device short-circuits its capacitive features, hindering any charge/discharge capacitive process. In addition, the high inductive artifacts and laser-related instability of the signal (e.g., temperature) further hinder the measurement of impedance spectroscopy in "pure" diffusion or high injection transport regimes. Since these additional contributions cannot be ruled out from the measurement data, the degree of proportionality between the extracted τ values and the effective recombination lifetimes remains indeterminate. Furthermore, it should be noted that impedance spectroscopy can only probe recombination processes within its sampling time window—typically those slower than the microsecond range. Consequently, faster processes, such as the minority-carrier lifetimes characteristic of GaAs devices,[39] cannot be accurately captured by this technique.

The impedance spectroscopy measurement under different illumination intensities for the 1 and 10 J devices is presented as Nyquist plots in Figs. 4(a) and 4(b). The obtained experimental spectra [dots in Figs. 4(a) and 4(b)] display a distinct "one-semicircle" pattern, indicating good agreement with the equivalent circuit models depicted in Fig. 1(c) and ruling out significant contributions from multiple transport mechanisms within the investigated frequency range.[36,40] The fitted data [lines in Figs. 4(a) and 4(b)] provide parameterized values for resistance, capacitance, and response times, which are plotted as functions of the incident photon power (P_{in}) in Figs. 4(c)–4(e) and the normalized photovoltage per sub-cell (V_{oc}/j) in Figs. 4(f)–4(h).
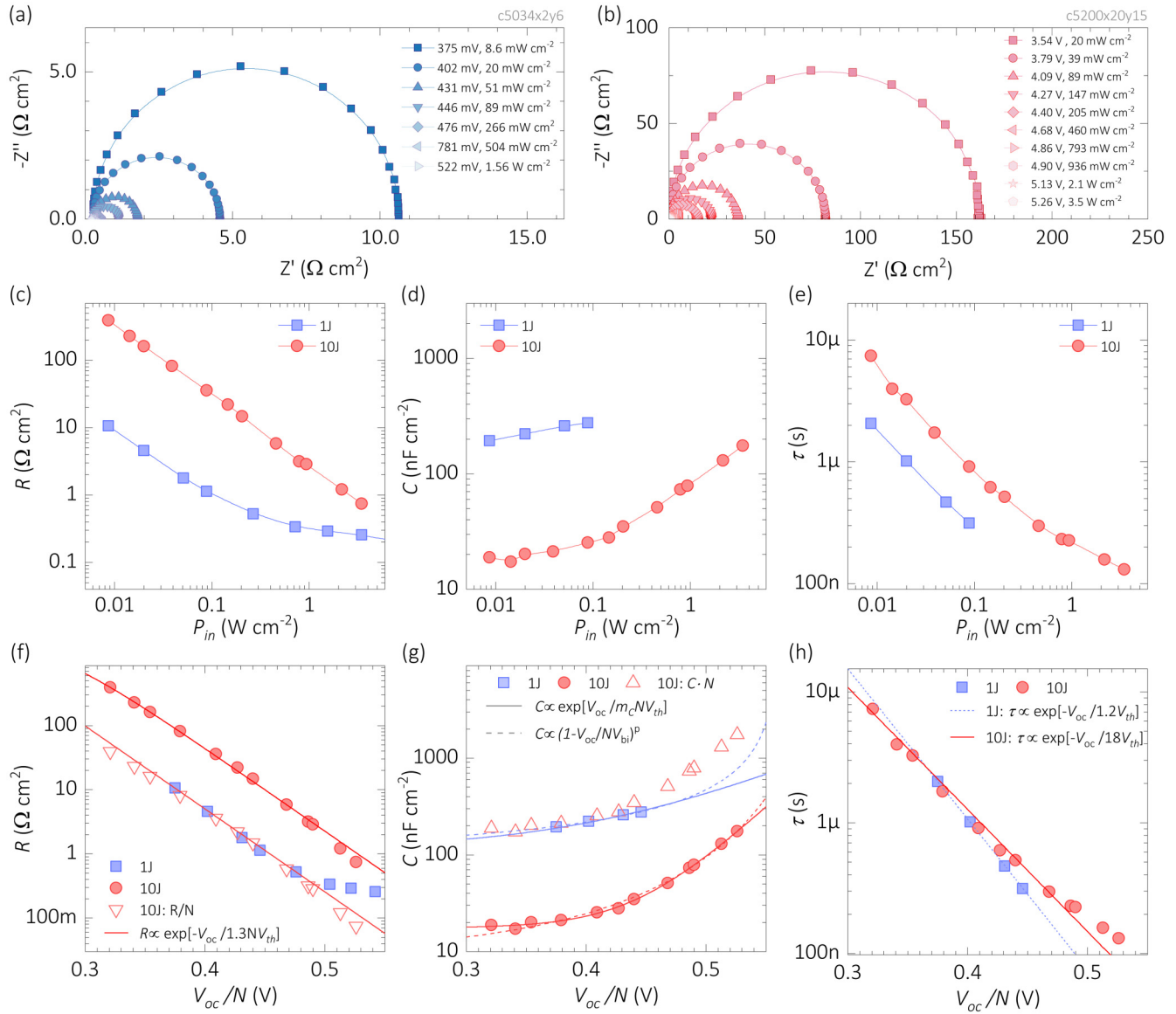
In terms of the incident irradiance, the resistance and capacitance values in Figs. 4(c) and 4(d) (solid symbols) are consistently higher and lower, respectively, for the 10 J device compared to those of the 1 J PPC. Notably, below 100 mW cm^{-2}, the resistance begins to deviate from its inverse decay trend ($R \propto P_{in}^{-1}$) and approaches a saturation toward the series resistance of the 1 J sample in Fig. 4(c). In this ohmic regime, capacitance measurements using the employed LCR meter are no longer feasible and the estimation of response times requires alternate methods, such as time-of-flight.[25,41] The inductive-like or negative capacitance dominates the imaginary part of impedance signal for these high values of irradiance/voltage, preventing the estimation of the capacitance, even though the resistance (real part of impedance) is well defined up to 3.5 W cm^{-2}. For higher irradiance intensities, the instrument was unable to resolve the spectra due to the low impedance of the sample that would require more specialized frequency response analyzers. Moreover, Fig. 4(d) reveals a power-law relationship $C \propto P_{in}^{\alpha}$ with $0.2 < \alpha < 0.6$, leading to an approximate trend $\tau = RC \propto P_{in}^{\alpha-1}$ for the resulting response times in Fig. 4(e). This indicates that the 10 J device requires nearly five times the irradiance of the 1 J sample to achieve the same characteristic response time. Moreover, the response time (τ) of the 10 J device is consistently higher than that of the 1 J PPC; for instance, under 88 mW cm^{-2}, irradiance, τ values are approximately 314 and 911 ns for the 1 and 10 J samples, respectively.

The analysis of the normalized photovoltage per sub-cell (V_{oc}/N) is presented in Figs. 4(f)–4(h). The sub-cell-normalized resistance values [open triangle symbols in Fig. 4(f)] for the 1 and 10 J samples follow the trend $R \propto \exp[-V_{oc}/(NmV_{th})]$, with $V_{th} = k_B T/q$ and $m \approx 1.3$ for $V_{oc}/N < 0.45$ V. This m value is slightly smaller than those shown in Fig. 2(b), suggesting that dark operation in the same forward-bias range may favor recombination within the space-charge region, compared to analogous quasi-open-circuit conditions under illumination.

In Fig. 4(g), the sub-cell-normalized capacitance of the 10 J sample is slightly higher than that of the 1 J sample when plotted as a function of the average sub-cell voltage. For the 1 J device, strong inductive artifacts under high irradiance conditions prevented reliable capacitance extraction and limited the accuracy of parameters describing the overall trends. The data were nonetheless fitted to examine the relation $C = C_0 + C_1(1 - V_{oc}/NV_{bi})^{-p}$, where V_{bi} is the built-in voltage and $C_{0,1}$, fitting parameter. A value $p > 0.5$ indicates a departure from depletion-layer capacitance, and for the 1 J sample, we obtained $p > 1$ [blue dashed line in Fig. 4(g)]. Although no clear exponential increase was observed—likely due to the inductive artifacts and the limited voltage range below flatband conditions—the 1 J data were also fitted to the form $C = C_0 + C_1\exp[V_{oc}/(Nm_C V_{th})]$, yielding $m_C \approx 3.3$ [blue solid line in Fig. 4(g)], albeit with low accuracy. By contrast, the 10 J device exhibits a much clearer exponential dependence, with $m_C = 1.47 \pm 0.02$ and $p > 2$ as shown by the red solid and dashed lines in Fig. 4(g), respectively.

Figure 4(h) shows good agreement between the response times from both samples at $V_{oc}/N < 0.45$ V. However, for higher V_{oc}/N values, the 10 J PPC exhibits greater τ than the 1 J sample, with the difference increasing alongside the photovoltage and the irradiance. This behavior is likely related to the capacitance [see Fig. 4(g)], as the resistance values in this range remain nearly identical [see in Fig. 4(f)]. This slight capacitance increase primarily indicates a higher average concentration of charge carriers for the 10 J sub-cells compared to that for the 1 J sub-cells. A primary reason for this could be the more effective photon management of the 10 J device including current matching and radiative coupling between sub-cells. In addition, from the point of view of the diffusion capacitance formalism, slight differences in the diffusion coefficient and/or average density of states due to heat distribution between sub-cells could also be contributing factors.[38,40]

The impedance spectroscopy results reveal distinct behaviors between 1 and 10 J full devices (solid dots in Fig. 4). The 10 J device exhibits longer response times, increased resistance, and reduced capacitance compared to the 1 J device at equivalent power densities as a consequence of the architecture and similarities between the properties of the sub-cells of the MJ device and those of the 1 J PPC. However, when analyzed per normalized sub-cell open-circuit voltage (open dots in Fig. 4), the resistances and response times of both devices are nearly identical under low irradiance conditions ($P_{in} < 30$ mW cm^{-2}, $V_{oc}/N < 0.4$ V). At higher irradiances ($P_{in} > 30$ mW cm^{-2}, $V_{oc}/N > 0.4$ V), the 10 J device shows increased capacitance and longer characteristic response times compared to the 1 J device. Despite the limited data following this behavior, we speculate on a transition in recombination mechanisms that favors the multi-junction device for energy conversion applications, where longer response times correlate with improved

FIG. 4. Impedance spectroscopy characterization in open-circuit conditions under different irradiance intensities of a 1520 nm laser. The Nyquist plots [(a) and (b)] for the experimental data (symbols) and corresponding fittings (lines) to the equivalent circuit model in Fig. 1 are shown for the single-junction (a) and the ten-junction (b) devices with lighter colors representing higher irradiance. The resulting parameterized resistance R [(c) and (f)], capacitance C [(d) and (g)], and characteristic response times τ [(e) and (h)] are plotted as functions of the incident power P_{in} [(c)–(e)] and the normalized open-circuit voltage per sub-cell V_{oc}/N [(f)–(h)].

PCE, but comes at the cost of slower response times. Other possible causes might be subtle differences between the 1 and 10 J device related to the length of the quasi-neutral regions compared to the diffusion length, i.e., depending on whether the diodes are working in the limit of short or long diodes. However, further investigation with an expanded statistical data set is necessary to elucidate this observation.

IV. CONCLUSIONS

Steady-state current–voltage and impedance measurements under dark and increasing monochromatic irradiances were employed to investigate power conversion efficiency, resistance, capacitance, and quasi-open-circuit response times in single-junction (1 J) and ten-junction (10 J) $In_{0.53}Ga_{0.47}As$ photonic power converters.

16 November 2025 15:43:12

A methodology for analyzing normalized sub-cell properties was introduced, enabling a more effective comparison between the two devices. The impedance spectroscopy analysis revealed the decrease and increase of resistance and capacitance of the 1 and 10 J devices, respectively, confirming their response time to scale with the number junctions in each device. At low irradiances, the individual sub-cells exhibit nearly identical resistance and capacitance behavior as well as response time, validating the average sub-cell approach used in the investigation. At irradiances above $100\,\text{mW cm}^{-2}$, sub-cells in the 10 J device exhibit a larger capacitance and consequently longer characteristic response times as compared to the 1 J device, highlighting a difference of the average recombination activity in the device.

AUTHOR DECLARATIONS

Conflict of Interest

The authors have no conflicts to disclose.

Author Contributions

Osbel Almora: Conceptualization (lead); Data curation (equal); Formal analysis (equal); Funding acquisition (lead); Investigation (equal); Methodology (lead); Project administration (lead); Resources (supporting); Software (equal); Supervision (equal); Validation (equal); Visualization (lead); Writing – original draft (lead); Writing – review & editing (lead). **Alexandre W. Walker:** Data curation (supporting); Formal analysis (equal); Investigation (equal); Project administration (equal); Resources (supporting); Software (equal); Supervision (supporting); Validation (equal); Visualization (supporting); Writing – review & editing (equal). **D. Paige Wilson:** Data curation (equal); Formal analysis (equal); Investigation (equal); Methodology (supporting); Software (supporting); Validation (supporting); Visualization (supporting); Writing – review & editing (supporting). **Carmine Pellegrino:** Data curation (equal); Formal analysis (equal); Investigation (supporting); Validation (equal); Visualization (equal); Writing – review & editing (equal). **Meghan N. Beattie:** Conceptualization (supporting); Investigation (supporting); Methodology (supporting); Writing – review & editing (supporting). **Lluis F. Marsal:** Conceptualization (supporting); Formal analysis (supporting); Funding acquisition (supporting); Supervision (supporting); Writing – review & editing (supporting). **David Lackner:** Resources (supporting); Validation (supporting); Writing – review & editing (supporting). **Henning Helmers:** Data curation (supporting); Funding acquisition (equal); Project administration (supporting); Resources (supporting); Supervision (supporting); Validation (supporting); Visualization (supporting); Writing – review & editing (equal). **Karin Hinzer:** Conceptualization (equal); Formal analysis (supporting); Funding acquisition (equal); Methodology (supporting); Project administration (equal); Resources (lead); Supervision (supporting); Validation (supporting); Visualization (supporting); Writing – review & editing (supporting).

DATA AVAILABILITY

The data that support the findings of this study are available from the corresponding authors upon reasonable request.

REFERENCES

[1]M. M. Wilkins, M. Ishigaki, P. O. Provost, D. Masson, S. Fafard, C. E. Valdivia, E. M. Dede, and K. Hinzer, "Ripple-free boost-mode power supply using photonic power conversion," IEEE Trans. Power Electron. **34**, 1054–1064 (2019).

[2]S. Fafard and D. P. Masson, "Perspective on photovoltaic optical power converters," J. Appl. Phys. **130**, 160901 (2021).

[3]C. Algora, I. García, M. Delgado, R. Peña, C. Vázquez, M. Hinojosa, and I. Rey-Stolle, "Beaming power: Photovoltaic laser power converters for power-by-light," Joule **6**, 340–368 (2022).

[4]L. C. Hirst and N. J. Ekins-Daukes, "Fundamental losses in solar cells," Prog. Photovoltaics **19**, 286–293 (2011).

[5]O. Höhn, A. W. Walker, A. W. Bett, and H. Helmers, "Determining the optimal laser wavelength for laser power conversion depending on operation temperature," Light Energy Environ. PTh4A.3 (2016).

[6]O. Höhn, A. W. Walker, A. W. Bett, and H. Helmers, "Optimal laser wavelength for efficient laser power converter operation over temperature," Appl. Phys. Lett. **108**, 241104 (2016).

[7]M. N. Beattie, M. Zamiri, K. L. C. Kaller, M. M. Wilkins, C. E. Valdivia, D. Xia, M. C. Tam, H. Kim, J. J. Krich, Z. Wasilewski, and K. Hinzer, "Two-junction III-V photonic power converter operating at monochromatic telecom wavelengths," in *2020 47th IEEE Photovoltaic Specialists Conference (PVSC)* (IEEE, 2020), pp. 1062–1066.

[8]S. Fafard, F. Proulx, M. C. A. York, L. S. Richard, P. O. Provost, R. Arès, V. Aimez, and D. P. Masson, "High-photovoltage GaAs vertical epitaxial monolithic heterostructures with 20 thin p/n junctions and a conversion efficiency of 60%," Appl. Phys. Lett. **109**, 131107 (2016).

[9]J. Schubert, E. Oliva, F. Dimroth, W. Guter, R. Loeckenhoff, and A. W. Bett, "High-voltage GaAs photovoltaic laser power converters," IEEE Trans. Electron Devices **56**, 170–175 (2009).

[10]H. Helmers, O. Höhn, D. Lackner, P. Schygulla, M. Klitzke, J. Schön, C. Pellegrino, E. Oliva, M. Schachtner, P. Beutel, S. Heckelmann, F. Predan, J. Ohlmann, G. Siefer, and F. Dimroth, "Advancing solar energy conversion efficiency to 47.6% and exploring the spectral versatility of III-V photonic power converters," Proc. SPIE **12881**, 1288103 (2024).

[11]H. Helmers, E. Lopez, O. Höhn, D. Lackner, J. Schön, M. Schauerte, M. Schachtner, F. Dimroth, and A. W. Bett, "68.9% efficient GaAs-based photonic power conversion enabled by photon recycling and optical resonance," Phys. Status Solidi RRL **15**, 2100113 (2021).

[12]N. A. Kalyuzhnyy, A. V. Malevskaya, S. A. Mintairov, M. A. Mintairov, M. V. Nakhimovich, R. A. Salii, M. Z. Shvarts, and V. M. Andreev, "Photovoltaic AlGaAs/GaAs devices for conversion of high-power density laser (800–860 nm) radiation," Sol. Energy Mater. Sol. Cells **262**, 112551 (2023).

[13]H. Helmers, E. Oliva, M. Schachtner, G. Mikolasch, L. A. Ruiz-Preciado, A. Franke, and J. Bartsch, "Overcoming optical-electrical grid design trade-offs for cm²-sized high-power GaAs photonic power converters by plating technology," Prog. Photovoltaics **32**, 636–642 (2024).

[14]M. N. Beattie, H. Helmers, G. P. Forcade, C. E. Valdivia, O. Höhn, and K. Hinzer, "InP- and GaAs-based photonic power converters under O-band laser illumination: Performance analysis and comparison," IEEE J. Photovoltaics **13**, 113–121 (2023).

[15]S. Fafard and D. Masson, "Vertical multi-junction laser power converters with 61% efficiency at 30 W output power and with tolerance to beam non-uniformity, partial illumination, and beam displacement," Photonics **10**, 940 (2023).

[16]C. Pellegrino, F. Dimroth, J. Ohlmann, H. Helmers, and D. Lackner, "InP-on-GaAs engineered substrates: A pathway toward low-cost, high-efficiency optoelectronic device fabrication," AIP Adv. **15**, 025319 (2025).

[17]J. Fakidis, H. Helmers, and H. Haas, "Simultaneous wireless data and power transfer for a 1-Gb/s GaAs VCSEL and photovoltaic link," IEEE Photonics Technol. Lett. **32**, 1277–1280 (2020).

[18]O. Almora, P. Lopez-Varo, K. T. Cho, S. Aghazada, W. Meng, Y. Hou, C. Echeverría-Arrondo, I. Zimmermann, G. J. Matt, J. A. Jiménez-Tejada, C. J. Brabec, M. K. Nazeeruddin, and G. Garcia-Belmonte, "Ionic dipolar switching hinders charge collection in perovskite solar cells with normal and inverted hysteresis," Sol. Energy Mater. Sol. Cells **195**, 291–298 (2019).

[19]E. Ghahremanirad, O. Almora, S. Suresh, A. A. Drew, T. H. Chowdhury, and A. R. Uhl, "Beyond protocols: Understanding the electrical behavior of perovskite solar cells by impedance spectroscopy," Adv. Energy Mater. **13**, 2204370 (2023).

[20]D. A. van Nijen, P. Procel, R. A. C. M. M. van Swaaij, M. Zeman, O. Isabella, and P. Manganiello, "The role of silicon PN junction impedance at high frequency," Sol. Energy Mater. Sol. Cells **282**, 113383 (2025).

[21]E. von Hauff, "Impedance spectroscopy for emerging photovoltaics," J. Phys. Chem. C **123**, 11329–11346 (2019).

[22]S. M. Sze and K. K. Ng, *Physics of Semiconductor Devices* (John Wiley & Sons, Hoboken, NJ, 2007), p. 832.

[23]A. Zhang and J. Gao, "Comprehensive analysis of linear and nonlinear equivalent circuit model for GaAs-PIN diode," IEEE Trans. Ind. Electron. **69**, 11541–11548 (2022).

[24]S. Soresi, G. Hamon, A. Larrue, J. Alvarez, M. P. Pires, and J. Decobert, "InP: S/AlInAs:C tunnel junction grown by MOVPE for photovoltaic applications," Phys. Status Solidi A **215**, 1700427 (2018).

[25]O. Almora, D. Miravet, M. García-Batlle, and G. Garcia-Belmonte, "Ballistic-like space-charge-limited currents in halide perovskites at room temperature," Appl. Phys. Lett. **119**, 242107 (2021).

[26]H. Helmers, O. Höhn, T. Tibbits, M. Schauerte, H. M. N. Amin, and D. Lackner, "Unlocking 1550 nm laser power conversion by InGaAs single- and multi-junction PV cells," in *2022 IEEE 49th Photovoltaics Specialists Conference (PVSC)* (IEEE, 2022), p. 1235.

[27]G. P. Forcade, D. P. Wilson, M. N. Beattie, C. Pellegrino, H. Helmers, R. F. H. Hunter, O. Höhn, D. Lackner, L.-P. St-Arnaud, T. N. D. Tibbits, C. E. Valdivia, Y. Grinberg, A. W. Walker, J. J. Krich, and K. Hinzer, "Multi-junction laser power converters exceeding 50% efficiency in the short wavelength infrared," Cell Rep. Phys. Sci. **6**, 102610 (2025).

[28]T. N. D. Tibbits, P. Beutel, M. Grave, C. Karcher, E. Oliva, G. Siefer, A. Wekkeli, M. Schachtner, F. Dimroth, A. W. Bett, R. K. Krause, M. Piccin, N. Blanc, M. Muñoz-Rico, C. J. Arena, E. Guiot, C. Charles-Alfred, C. Drazek, F. Janin, L. Farrugia, B. Hoarau, J. Wasselin, A. Tauzin, T. Signamarcheix, T. Hannappel, K. Schwarzburg, and A. Dobrich, "New efficiency frontiers with wafer bonded multi-junction solar cells," in *29th European Photovoltaic Solar Energy Conference (EU PVSEC) 2014, Session 4CP.2.1* (WIP GmbH & Co. Plaungs-KG, 2014), pp. 1975–1978.

[29]G. P. Forcade, M. N. Beattie, C. E. Valdivia, H. Helmers, O. Höhn, P. Wilson, L. P. St-Arnaud, R. Hunter, D. Lackner, J. J. Krich, A. W. Walker, and K. Hinzer, "High-performance multi-junction C-band photonic power converters: Calibrated optoelectronic model for next generation designs," in *2023 IEEE 50th Photovoltaic Specialists Conference (PVSC)* (IEEE, 2023), p. 1.

[30]M. Wilkins, C. E. Valdivia, A. M. Gabr, D. Masson, S. Fafard, and K. Hinzer, "Luminescent coupling in planar opto-electronic devices," J. Appl. Phys. **118**, 143102 (2015).

[31]O. Almora, K. T. Cho, S. Aghazada, I. Zimmermann, G. J. Matt, C. J. Brabec, M. K. Nazeeruddin, and G. Garcia-Belmonte, "Discerning recombination mechanisms and ideality factors through impedance analysis of high-efficiency perovskite solar cells," Nano Energy **48**, 63–72 (2018).

[32]J. Bisquert, *Nanostructured Energy Devices: Equilibrium Concepts and Kinetics* (CRC Press, Boca Raton, 2014).

[33]A. Niemegeers and M. Burgelman, "Effects of the Au/CdTe back contact on IV and CV characteristics of Au/CdTe/CdS/TCO solar cells," J. Appl. Phys. **81**, 2881–2886 (1997).

[34]S. Fafard and D. Masson, "Onset of quantum-confined stark effects in multi-junction photovoltaic laser power converters designed with thin subcells," Photonics **10**, 1243 (2023).

[35]J. Bisquert, "Chemical capacitance of nanostructured semiconductors: Its origin and significance for nanocomposite solar cells," Phys. Chem. Chem. Phys. **5**, 5360–5364 (2003).

[36]O. Almora, Y. Zhao, X. Du, T. Heumueller, G. J. Matt, G. Garcia-Belmonte, and C. J. Brabec, "Light intensity modulated impedance spectroscopy (LIMIS) in all-solid-state solar cells at open-circuit," Nano Energy **75**, 104982 (2020).

[37]J. Bisquert, "Interpretation of the recombination lifetime in halide perovskite devices by correlated techniques," J. Phys. Chem. Lett. **13**, 7320–7335 (2022).

[38]O. Almora and G. Garcia-Belmonte, "Light capacitances in silicon and perovskite solar cells," Sol. Energy **189**, 103–110 (2019).

[39]M. Niemeyer, J. Ohlmann, A. W. Walker, P. Kleinschmidt, R. Lang, T. Hannappel, F. Dimroth, and D. Lackner, "Minority carrier diffusion length, lifetime and mobility in p-type GaAs and GaInAs," J. Appl. Phys. **122**, 115702 (2017).

[40]O. Almora, L. G. Gerling, C. Voz, R. Alcubilla, J. Puigdollers, and G. Garcia-Belmonte, "Superior performance of V$_2$O$_5$ as hole selective contact over other transition metal oxides in silicon heterojunction solar cells," Sol. Energy Mater. Sol. Cells **168**, 221–226 (2017).

[41]O. Almora, G. J. Matt, A. These, A. Kanak, I. Levchuk, S. Shrestha, A. Osvet, C. J. Brabec, and G. Garcia-Belmonte, "Surface versus bulk currents and ionic space-charge effects in CsPbBr$_3$ single crystals," J. Phys. Chem. Lett. **13**, 3824–3830 (2022).

16 November 2025 15:43:12